Monthly Notices of the ROYAL ASTRONOMICAL SOCIETY

MNRAS **515,** 3028–3036 (2022) https://doi.org/10.1093/mnras/stac1366
Advance Access publication 2022 May 18

Shocks and dust formation in nova V809 Cep

Aliya-Nur Babul,[1] Jennifer L. Sokoloski,[1]★ Laura Chomiuk,[2] Justin D. Linford,[3] Jennifer H. S. Weston,[4] Elias Aydi,[2] Kirill V. Sokolovsky ,[2,5] Adam M. Kawash[2] and Koji Mukai[6,7]

[1]*Department of Astronomy, Columbia University, 550 West 120th Street, New York, NY 10027, USA*
[2]*Center for Data Intensive and Time Domain Astronomy, Department of Physics and Astronomy, Michigan State University, East Lansing, MI 48824, USA*
[3]*National Radio Astronomy Observatory, PO Box O, Socorro, NM 87801, USA*
[4]*Federated IT, 1201 Wilson Blvd, 27th Floor, Arlington, VA 22209, USA*
[5]*Sternberg Astronomical Institute, Moscow State University, Universitetskii pr. 13, 119992 Moscow, Russia*
[6]*CRESST and X-ray Astrophysics Laboratory, NASA Goddard Space Flight Center, Greenbelt, MD 20771, USA*
[7]*Department of Physics, University of Maryland, Baltimore County, 1000 Hilltop Circle, Baltimore, MD 21250, USA*

Accepted 2022 April 29. Received 2022 April 29; in original form 2021 June 29

ABSTRACT

The discovery that many classical novae produce detectable GeV γ-ray emission has raised the question of the role of shocks in nova eruptions. Here, we use radio observations of nova V809 Cep (nova Cep 2013) with the Jansky Very Large Array to show that it produced non-thermal emission indicative of particle acceleration in strong shocks for more than a month starting about 6 weeks into the eruption, quasi-simultaneous with the production of dust. Broadly speaking, the radio emission at late times – more than 6 months or so into the eruption – is consistent with thermal emission from 10^{-4} $M_\odot$ of freely expanding, 10^4 K ejecta. At 4.6 and 7.4 GHz, however, the radio light curves display an initial early-time peak 76 d after the discovery of the eruption in the optical (t_0). The brightness temperature at 4.6 GHz on day 76 was greater than 10^5 K, an order of magnitude above what is expected for thermal emission. We argue that the brightness temperature is the result of synchrotron emission due to internal shocks within the ejecta. The evolution of the radio spectrum was consistent with synchrotron emission that peaked at high frequencies before low frequencies, suggesting that the synchrotron from the shock was initially subject to free–free absorption by optically thick ionized material in front of the shock. Dust formation began around day 37, and we suggest that internal shocks in the ejecta were established prior to dust formation and caused the nucleation of dust.

Key words: acceleration of particles – radiation mechanisms: non-thermal – shock waves – stars: individual: V809 Cep – radio continuum: transients – novae, cataclysmic variables.

1 INTRODUCTION

A classical nova is an eruption that occurs in an interacting stellar binary system in which one star is a white dwarf and the other is typically a main-sequence star (Chomiuk, Metzger & Shen 2021; Della Valle & Izzo 2020). Hydrogen-rich material from the donor star accretes on to the white dwarf and is compressed, causing the temperature to rise. The soaring temperatures trigger a thermonuclear runaway and a subsequent ejection of matter from the white dwarf (e.g., Starrfield, Iliadis & Hix 2016). As material is ejected from the white dwarf, the system brightens across much of the electromagnetic spectrum, allowing for the discovery of such phenomenon.

Between its launch in 2008 June and 2021 April, the Large Area Telescope (LAT; Atwood et al. 2009) of the *Fermi Gamma Ray Space Telescope* detected GeV γ-rays from 17 novae (see the list in Franckowiak et al. 2018; Chomiuk, Metzger & Shen 2021, plus the recurrent nova V3890 Sgr; Buson, Jean & Cheung 2019), typically within a few days of their optical peak (e.g. Ackermann et al. 2014; Chomiuk et al. 2021). The presence of GeV γ-rays implies that these eruptions have generated a population of relativistic particles. These particles are likely produced via the diffusive shock acceleration mechanism as a result of internal shocks within the ejecta (e.g. Blandford 1994; Metzger et al. 2016). The high-energy particles may produce γ-rays via a number of processes, including pion decay, inverse Compton scattering of ambient optical photons, and relativistic bremsstrahlung (Metzger et al. 2015; Martin et al. 2018). High-energy particles may also produce synchrotron radiation in the radio band (Vlasov, Vurm & Metzger 2016). Radio imaging of nova V959 Mon revealed regions of synchrotron emission, further confirming the presence of shocks and providing a localization within the ejecta. From the images, Chomiuk et al. (2014a) postulated that the shocks are the result of collisions between two outflows from the white dwarf: the first, more slowly moving outflow having a toroidal geometry, and the second, faster flow having a more spherical geometry. The shocks were located near the equatorial plane, where the two outflows collided. Based on the optical spectral evolution of a large sample of novae, Aydi et al. (2020a) found consistent evidence for this colliding outflows scenario. Finally, observations of correlated variations in GeV and optical brightness suggest that shocks may transport a significant fraction of the nova eruption energy (Li et al. 2017; Aydi et al. 2020b) and power a substantial

★ E-mail: jeno@astro.columbia.edu

fraction of the bolometric luminosity during the early weeks of a nova eruption.

In nova-producing binaries that are too distant for γ-ray detections, radio observations provide a unique opportunity to study developing shocks. Radio light curves sometimes contain local maxima, which we refer to as *early-time flares*, within months of the initial optical peak (Taylor et al. 1987; Weston et al. 2016a; Finzell et al. 2018). These early-time flares correspond to radio surface brightnesses (parametrized as brightness temperatures) that are at least an order of magnitude higher than expected from thermally emitting, 10^4 K ionized gas that is expanding freely with speeds inferred from optical spectral lines (Cunningham, Wolf & Bildsten 2015). Because the brightness temperature represents a lower limit on the temperature of thermally emitting material, brightness temperatures in excess of 10^5 K indicate that either the ejecta contain enough $T \geq 10^5$ K gas for that gas to be optically thick to free–free emission at radio wavelengths or the radio emission is non-thermal emission from electrons accelerated via shocks. In at least one case (V1723 Aql), Weston et al. (2016a) argued that the mass of 10^5 K gas required for the ejecta to generate the observed radio emission through thermal processes was unfeasible, and that the high brightness temperature was more likely to be the result of synchrotron emission produced near the internal shocks in the ejecta (Vlasov et al. 2016).

Optical and infrared (IR) light curves of classical novae sometimes display characteristics of dust formation days to months after the initial eruption (e.g. Evans 2001; Shore et al. 2018). Sudden decreases in the optical flux are seen in about 20 percent of novae within 100 d of the optical peak (Strope, Schaefer & Henden 2010). These decreases occur earlier than what would be expected due to the natural fading in nova luminosity over time, and – along with the subsequent optical rebrightenings – are referred to as 'dust dips'. They result from the obscuring of some optical light from the nova due to the formation of dust and also often appear along with brightening at IR wavelengths, a typical signature of dust emission (Gehrz 2008).

Dust production requires cool ($T \lesssim 10^3$ K) gas for the condensation of dust grains, and regions of dust condensation must be shielded from the ionizing radiation emanating from the white dwarf. Derdzinski, Metzger & Lazzati (2017) and Gallagher (1977) reconcile the presence of harsh radiation with the onset of dust formation. Their model, which we refer to as the *shock–dust model*, postulates that dense radiative shocks, such as the ones thought to give rise to the γ-rays and early-time radio peaks, provide the optimal conditions for dust condensation. As both the forward and reverse shocks progress, the gas density behind the shocks increases rapidly, producing a thin shell of dense gas between the forward and reverse shocks (Vlasov et al. 2016; Steinberg & Metzger 2018). This shell is dense enough to be protected from radiation, and as the gas cools, molecules can begin to nucleate into dust particles. Because radio imaging shows that shocks are produced at the interface between the slow-moving toroidal outflow and the fast-moving spherical outflow, the dense shells (and dust formation) might be localized in the equatorial plane.

V809 Cep was first discovered in a nova eruption on 2013 February 2 by K. Nishiyama and F. Kabashima (CBET 3397), and we take this date to be the start of the eruption, t_0. V809 Cep reached peak optical brightness 1 d later (Munari et al. 2014). Emission-line profiles on days 220 and 352 for [O III] 5007 Å and [N II] 6548, 6584 + Hα had a double peak with a separation of 1160 km s^{-1} corresponding to a bulk velocity of 600 km s^{-1} (Munari et al. 2014). Using the Echelle spectra and comparing with Brand & Blitz (1993), Munari et al. (2014) found the lower limit on the distance to be 6 kpc associated with the crossing of the Perseus or outer arm. Additionally, using methods from Downes & Duerbeck (2000) and maximum magnitude vs rate of decline (MMRD) techniques, they refined their distance estimate to 6.5 kpc. We thus take the distance to be $D = 6.5$ kpc.

Table 1. V809 Cep radio observations.

Date	$t - t_0$[a]	MJD	Epoch	Configuration	Bands observed	Time (min)[b]
02/14/2013	12	56337.0	1	D	*C*, *Ka*	47.9
03/22/2013	48	56373.5	2	D	*C*, *Ka*	47.9
04/04/2013	61	56386.9	3	D	*C*, *Ka*	47.9
04/19/2013	76	56401.6	4	D	*C*, *Ka*	29.9
05/23/2013	110	56435.4	5	C	*C*, *U*, *Ka*	29.9
06/10/2013	128	56453.5	6	C	*C*, *U*, *Ka*	29.9
06/16/2013	134	56459.3	7	C	*C*, *U*, *Ka*	29.9
07/05/2013	153	56478.3	8	C	*C*, *U*, *Ka*	29.9
08/27/2013	206	56531.2	9	C	*C*, *U*, *Ka*	29.9
09/27/2013	237	56562.2	10	B	*C*, *U*, *Ka*	29.2
11/22/2013	293	56618.0	11	B	*C*, *U*, *Ka*	29.9
11/30/2013	301	56626.8	12	B	*C*, *U*, *Ka*	29.9
12/16/2013	317	56642.8	13	B	*C*, *U*, *Ka*	29.9
03/14/2014	405	56719.7	14	A	*C*, *U*, *Ka*	29.9
04/29/2014	451	56776.5	15	A	*C*, *U*, *Ka*	30.2
05/28/2014	480	56805.6	16	A	*C*, *U*, *Ka*	30.2
07/08/2014	521	56846.3	17	D	*C*, *U*, *Ka*	29.9
09/06/2014	581	56906.2	18	D	*C*, *U*, *Ka*	29.9
11/07/2014	642	56968.0	19	C	*C*, *U*, *Ka*	29.9
01/29/2015	726	57051.1	20	B	*C*, *U*, *Ka*	27.4
04/21/2015	808	57133.5	21	B	*C*, *U*, *Ka*	29.9
09/06/2015	946	57271.4	22	A	*Ka*, *U*, *S*, *C*	31.4
01/28/2016	1090	57415.0	23	C	*Ka*, *U*, *S*, *C*	38.6

[a]We take the start time of the eruption, t_0, to be 2013 February 2.
[b]Total time on source.

In this paper, we use radio observations to show that nova V809 Cep produced non-thermal emission quasi-simultaneously with dust production. We postulate that the non-thermal emission occurred prior to the dust formation, but was initially absorbed by photoionized gas ahead of the shock. In Section 2, we describe the technical details of the observations and data reduction. In Section 3, we present our results, and in Section 4 we discuss the implications of our findings in validating the shock–dust model.

2 OBSERVATIONS

We monitored V809 Cep using the Karl G. Jansky Very Large Array Telescope (VLA) between 2013 February 14 and 2016 January 28 under programmes 13A-455, 13B-057, and 15B-343. Between 2013 February and 2016 January, the VLA cycled through all configurations (A, B, C, and D), and observed V809 Cep at *C* band (4–8 GHz), *Ku* band (12–18 GHz), and *Ka* band (26–40 GHz). All the observations from 2013 February to 2015 April were performed in the 8-bit observing mode with 2-GHz bandwidth at all bands. The observations in 2015 September and 2016 January were performed in the 3-bit mode with 4-GHz bandwidth at *C* band, 6-GHz bandwidth at *Ku* band, and 8-GHz bandwidth at *Ka* band. Table 1 lists details for each observation.

For observations carried out prior to 2013 May, we reduced the data using AIPS (Greisen 2003). For observations carried out between 2013 May and 2016 May, we reduced the data using standard routines in CASA (McMullin et al. 2007). To obtain radio flux densities, we fit an elliptical Gaussian to the source image using `JMFIT` in AIPS and `gaussfit` in CASA. V809 Cep appeared as an unresolved point source at all epochs; therefore, the VLA configuration had no effect on the flux densities obtained using AIPS and CASA. We estimated uncertainties in the flux density by adding in quadrature the uncertainty from the fit with a systematic uncertainty from absolute

Table 2. V809 Cep radio flux densities measured with the VLA between 2013 February 14 to 2016 January 28, in mJy.

Epoch	4.6 GHz	7.4 GHz	13.5 GHz	17.4 GHz	28.2 GHz	36.5 GHz
1	<0.051[a]	<0.018[a]	–	–	<0.031[a]	<0.039[a]
2	0.052 ± 0.016[b]	0.189 ± 0.020	–	–	0.696 ± 0.040	0.718 ± 0.051
3	0.229 ± 0.027	0.503 ± 0.032	–	–	1.00 ± 0.028	0.926 ± 0.037
4	0.410 ± 0.061	0.627 ± 0.016	0.789 ± 0.015	0.942 ± 0.017	1.521 ± 0.031	2.143 ± 0.057
5	<0.054[a]	0.334 ± 0.029	0.814 ± 0.025	1.150 ± 0.022	2.639 ± 0.065	3.809 ± 0.097
6	0.240 ± 0.027	0.434 ± 0.014	1.08 ± 0.015	1.56 ± 0.015	3.25 ± 0.039	4.69 ± 0.058
7	0.260 ± 0.033	0.542 ± 0.021	1.05 ± 0.017	1.48 ± 0.021	3.39 ± 0.0608	4.40 ± 0.082
8	0.252 ± 0.039	0.501 ± 0.015	1.366 ± 0.021	1.992 ± 0.024	4.228 ± 0.077	6.05 ± 0.12
9	0.287 ± 0.025	0.650 ± 0.024	1.583 ± 0.024	2.419 ± 0.035	3.33 ± 0.01	4.51 ± 0.03
10	0.292 ± 0.019	0.515 ± 0.030	1.494 ± 0.037	1.797 ± 0.089	3.40 ± 0.13	3.37 ± 0.12
11	0.448 ± 0.018	0.820 ± 0.013	1.98 ± 0.02	2.55 ± 0.02	3.79 ± 0.05	3.87 ± 0.07
12	0.417 ± 0.023	0.831 ± 0.015	1.88 ± 0.02	2.28 ± 0.02	3.19 ± 0.04	3.03 ± 0.05
13	0.380 ± 0.023	0.902 ± 0.016	2.04 ± 0.02	2.66 ± 0.02	3.72 ± 0.06	3.47 ± 0.08
14	0.492 ± 0.017	0.916 ± 0.012	1.697 ± 0.013	1.907 ± 0.017	2.314 ± 0.040	2.187 ± 0.065
15	0.513 ± 0.027	0.896 ± 0.014	1.34 ± 0.01	1.48 ± 0.02	1.55 ± 0.02[e]	1.44 ± 0.03
16	0.495 ± 0.017	0.854 ± 0.011	1.22 ± 0.02	1.22 ± 0.02	1.26 ± 0.03[e]	1.16 ± 0.03
17	0.458 ± 0.037	0.903 ± 0.029	1.09 ± 0.02	1.20 ± 0.03	1.20 ± 0.05	1.26 ± 0.08
18	0.526 ± 0.033	0.765 ± 0.024	0.904 ± 0.020	0.952 ± 0.025	0.980 ± 0.062	0.887 ± 0.072
19	0.492 ± 0.024	0.667 ± 0.014	0.713 ± 0.015	0.688 ± 0.017	0.697 ± 0.043	0.620 ± 0.051
20	0.437 ± 0.034	0.503 ± 0.022	0.515 ± 0.022	0.523 ± 0.022	0.456 ± 0.044	0.351 ± 0.062
21	0.413 ± 0.020	0.432 ± 0.015	0.402 ± 0.015	0.382 ± 0.018	0.458 ± 0.042	0.549 ± 0.057
22	0.265 ± 0.013[c]	0.243 ± 0.012[d]	0.288 ± 0.022	0.311 ± 0.032[f]	0.234 ± 0.079[e]	0.124 ± 0.071[g]
23	0.305 ± 0.024[c]	0.203 ± 0.014[d]	0.176 ± 0.015	0.165 ± 0.011[f]	0.191 ± 0.024[e]	0.092 ± 0.025[g]

[a]We take the threshold for detection to be a flux density of at least three times the uncertainty (3σ). We list non-detections as 2σ upper limits.
[b]The flux density reported is measured at 4.7 GHz.
[c]The flux density reported is measured at 5.0 GHz.
[d]The flux density reported is measured at 7.0 GHz.
[e]The flux density reported is measured at 16.5 GHz.
[f]The flux density reported is measured at 29.5 GHz.
[g]The flux density reported is measured at 35.0 GHz.

flux calibration. At frequencies above 10 GHz, we took the absolute flux density uncertainty to be 10 per cent, and at frequencies below 10 GHz, we took the uncertainty introduced by the calibration to be 5 per cent. During each observation of V809 Cep, we also observed the source J2339+6010 and source 3C 48. Source J2339+6010 was used for complex gain calibration and source 3C 48 was used for absolute flux calibration.

Table 2 presents the flux densities and associated uncertainties. We take a measured flux density of between three and five times the total uncertainty to be a low-significance detection and a measured flux density of at least five times the total uncertainty to be a high-significance detection. Error bars correspond to 1σ uncertainties. For a given band, the frequency at which the observation takes place can fluctuate slightly so Table 2 also notes the exact frequency of the observation.

3 RESULTS

At high radio frequencies, roughly speaking, the flux density rose over the course of 5–10 months, and then faded, but at low frequencies, V809 Cep brightened and faded twice (Fig. 1). On 2013 March 22 (day 48 – Epoch 2), 5 weeks after a non-detection on 2013 February 14 (day 12-Epoch 1), the VLA detected V809 Cep at 7.4, 28.2, and 36.5 GHz. The source continued to brighten and was detected at all observed frequencies (4.6, 7.4, 28.2, and 36.5 GHz) on 2013 April 19. On day 76 (Epoch 4), the brightness at 4.6 and 7.4 GHz reached local maxima (Fig. 1), at flux densities of 0.41 ± 0.06 mJy and 0.63 ± 0.02 mJy, respectively (see Fig. 1 and Table 2). We refer to this low frequency brightening two to three months after the initial outburst as the early-time flare. Even during the decay of the flare, the flux densities at high frequencies continued to rise and reached maxima between days 100 and 300 before beginning to decline (see Fig. 1).

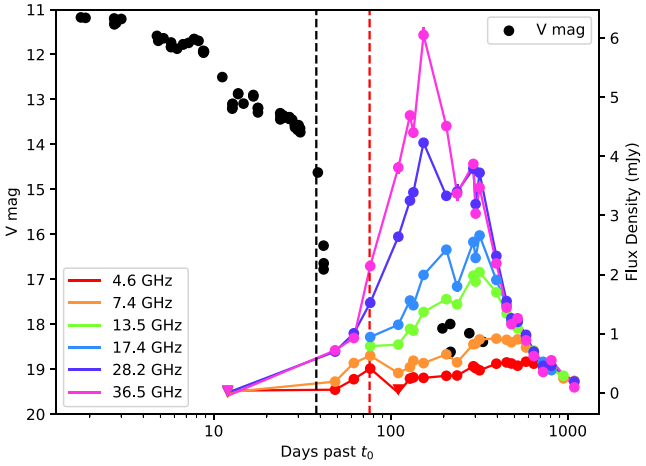

Figure 1. Optical and multifrequency radio light curves of nova V809 Cep as a function of days past discovery in the optical on 2013 February 2 (t_0). The triangles denote upper limits, and circles denote detections with significance of at least 3σ. The high-frequency radio light curves peak between days 100 and 300 (Epochs 5–12), and there is a local maximum on day 76 (Epoch 4) at 4.6 and 7.3 GHz (red vertical line). Black points are *V*-band magnitudes from Munari et al. (2014). Error bars are typically smaller than the points. The vertical black line denotes the onset of dust formation on day 37.

The radio spectrum evolved through four distinct stages: (1) a broken power law during the rise of the early-time flare; (2) a simple power law between epochs 5 and 8 (days 110–153), with a spectral index that remained stable at around $\alpha = 1.5$–1.6 for more than a month as the radio emission brightened again (taking $S_\nu \propto \nu^\alpha$, where S_ν is the flux density at frequency ν); (3) a broken power law again as the main decline started first at the highest and then lower frequencies; and (4) a simple, flat spectrum during the final decline. Fig. 2 shows the radio spectral energy distribution for selected epochs between 2013 March 22 and 2016 January 28. Over the full 3-yr timescale of the eruption – from 2013 March 22 (day 48) to 2016 January 28 (day 1090) – the radio spectrum evolved from one in which flux density increased with frequency, as expected for optically thick emitting material, to one in which flux density decreased slightly with frequency. We obtained the spectral index (α) for a given date and frequency range by performing a linear regression using SCIPY's least-squares curve fitting method in log–log space, taking into account the uncertainties in the flux density measurements. We generally split the frequencies into low frequencies (4.6 and 7.4 GHz), intermediate frequencies (13.5 and 17.4 GHz), and high frequencies (28.2 and 36.5 GHz). If the spectral indices at low, intermediate, and high frequencies were within 0.2 of each other, we fit them with a single power law. If the spectral indices differed by more than 0.2, we fit the spectrum with a broken power law.

During Epochs 2–4 (stage 1), the spectral index at low frequencies (4.6 and 7.4 GHz) differed from that at high frequencies. At low frequencies, the spectral index evolved from $\alpha = 2.8 \pm 0.7$ in Epoch 2 to a much flatter $\alpha = 0.48 \pm 0.07$ in Epoch 4. In contrast, at high frequencies the spectral index evolved from being quite flat at Epoch 2 ($\alpha = 0.1 \pm 0.4$) to rising with $\alpha = 1.5 \pm 0.2$ at Epoch 4. During stage 3 (Epochs 10–16), the spectrum flattened first at the highest frequencies (Epoch 10) and subsequently at lower frequencies, leading to stage 4 (Epochs 18–22), during which time the spectrum was flat ($\alpha = 0.1 \pm 0.1$ at Epoch 22) across the full range of frequencies.

4 DISCUSSION

4.1 Early-time radio flare

During the second and third month of the outburst, the nova produced a flare of low-frequency radio emission that we demonstrate below brightened more quickly than expected for freely expanding thermal ejecta and reached a brightness that exceeded expectations for thermally emitting material expanding at the speed of the principal optical absorbing system, suggesting that the flare was non-thermal in origin. The first piece of evidence in support of non-thermal emission is the rapid brightening at low frequencies. Between Epochs 2 and 3, the 4.6-GHz emission increased roughly as t^6, where t here is the time since t_0. Even if the material that generated the early-time flare was not ejected from the region of the white dwarf until 4 d after the start of the eruption (Munari et al. 2014), the 4.6-GHz flux density increased faster than t^4. During the same interval, the 7.4-GHz brightness increased as t^4. Between Epochs 3 and 4, the 4.6-GHz emission continued to increase faster than t^2. For a freely expanding blackbody with constant temperature, the brightness of thermal radio emission can only increase as fast as t^2, proportional to the increasing area of the source on the sky. Although it would be possible for the size of a thermally emitting source to increase faster than t^2 if an ionization front was rapidly propagating through the ejecta, or if the electron temperature of the emitting material was increasing, the high radio brightness during Epochs 3 and 4 (see discussion below and Fig. 3) disfavours either of these possibilities.

The second piece of evidence in support of non-thermal emission is the strength of the low-frequency radio emission during Epochs 3 and 4. We parametrize the radio flux density in terms of a *brightness temperature,* T_b – the minimum electron temperature required for the observed radio emission to arise from thermal bremsstrahlung. Brightness temperature is a measure of surface brightness. If a uniform temperature, bremsstrahlung-emitting medium is optically thick over its full area on the sky, the brightness temperature corresponds to its physical temperature; however, if it is even partially optically thin, or if the radio emission emanates from a region that is smaller than the size of the putative spherical ejecta, then the brightness temperature only provides a lower limit for the physical temperature. Assuming a spherically expanding shell, T_b is given by

$$T_\mathrm{b}(\nu, t) = \frac{S_\nu(t) c^2 D^2}{2\pi k_\mathrm{b} \nu^2 (v_\mathrm{ej} t)^2}, \quad (1)$$

where c is the speed of light, k_b is the Boltzmann constant, t is the time since t_0, and v_ej is the maximum expansion velocity. Using a distance of $D = 6.5$ kpc and a maximum ejection velocity of 1200 km s^{-1} (corresponding roughly to the faster of the two principal absorption systems seen in optical spectroscopy; Munari et al. 2014), the brightness temperature at 4.6 GHz reached $1.3 \pm 0.2 \times 10^5$ K [Epoch 4 (day 76); see Fig. 3]. For the early-time radio flare to have had a thermal origin would therefore require that on day 76 (Epoch 4), the ejecta included a shell of material with an electron temperature of at least 10^5 K, that was at least as extended on the sky as the 1200 km s^{-1} flow, and that was dense enough to be optically thick at 4.6 GHz. If the radio emission emanated from knots, or a portion of the ejecta that subtended a smaller solid angle on the sky than the 1200 km s^{-1} flow, the required electron temperature for the early-time flare to have been thermal is even higher. We argue below that such a large, hot, dense ejecta on day 76 (Epoch 4) seems unlikely.

Crucially, given that $T \sim 10^4$ K is the approximate equilibrium temperature for a plasma cooled by forbidden emission lines (e.g., Weston et al. 2016a), photoionized ejecta from novae are typically expected to have electron temperatures of around this value. In fact, Cunningham et al. (2015) found that for a wide range of white dwarf masses, ejecta masses, and ejecta speeds, the temperature of the photoionized ejecta generally does not exceed a few times 10^4 K at any point. It is possible that the peak brightness of the early-time radio flare in V809 Cep could have been generated by the most spatially extended flow associated with the so-called diffuse enhanced optical spectroscopic system (which had speeds of up to 2000 km s^{-1}, Munari et al. 2014) if it had a temperature of 4×10^4 K and was completely optically thick. However, the low-frequency spectral index on day 76 (Epoch 4) was $\alpha = 0.5 \pm 0.1$, much lower than the $\alpha \approx 2$ expected for optically thick bremsstrahlung, indicating that the radio-emitting ejecta were *not* optically thick at that time.

The expected temperature for photoionized ejecta and the $\alpha = 0.5$ spectral index thus both argue against a thermal origin for the early-time flare.

The high T_b is also unlikely to be due to a shell of shock-heated, 10^5 K gas between the forward and reverse shocks. Steinberg & Metzger (2018) explore the possibility of forward and reverse shocks in the ejecta producing a shell of cool ($\sim 10^4$ K), dense gas bounded by a shell of $T \sim 10^6$ K gas. We define $M_\mathrm{hot,needed}$ as the mass of 10^5 K gas that would be needed to make a shell of width L_cool optically thick at radio frequencies and $M_\mathrm{hot,expected}$ as the mass of 10^5 K gas theoretically expected to be present. Below, we compare $M_\mathrm{hot,expected}$ and $M_\mathrm{hot,needed}$.

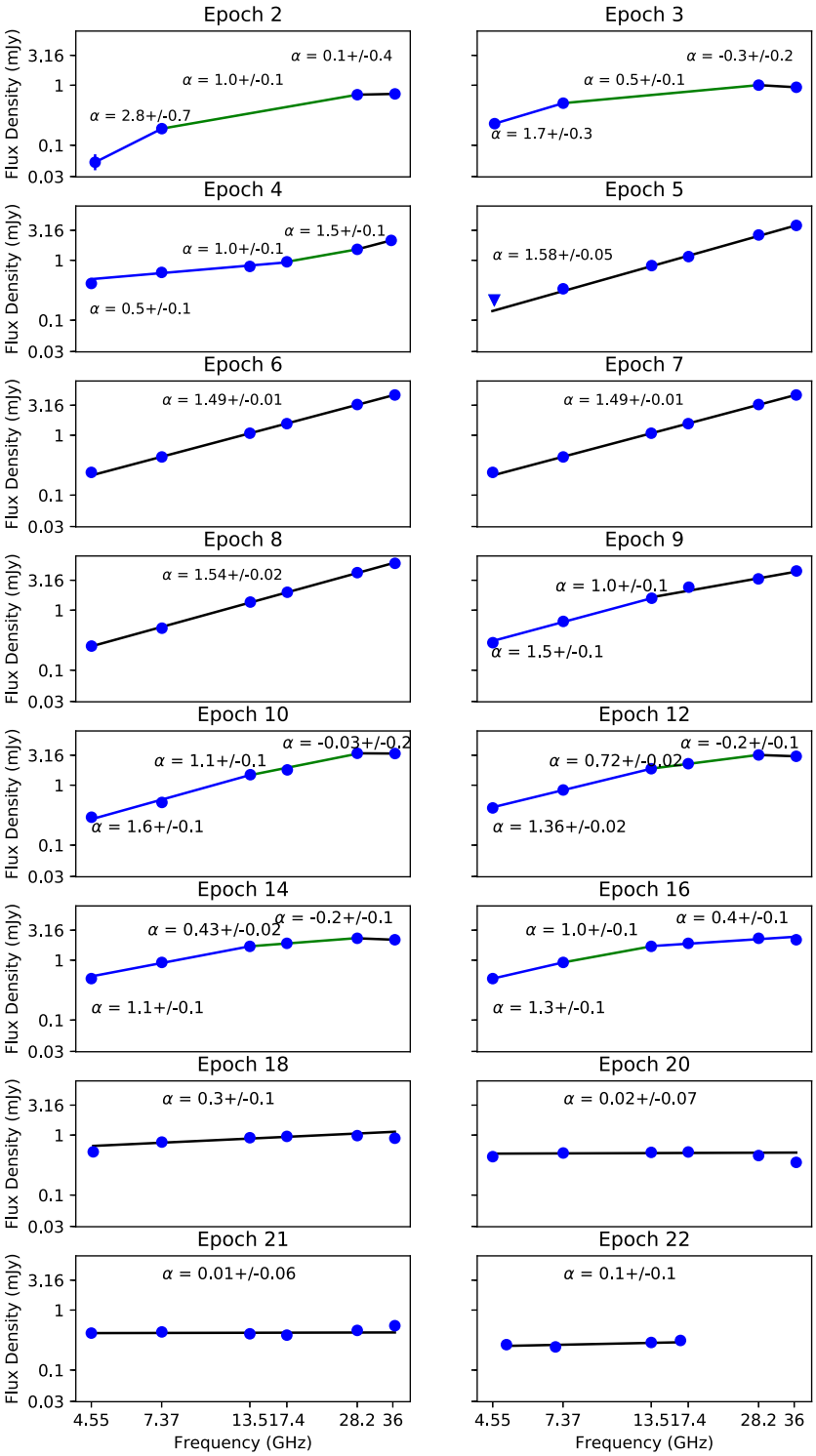

Figure 2. Evolution of the spectral energy distribution of V809 Cep for selected epochs between Epochs 1 and 23. Upper limits are plotted as triangles, and error bars are typically smaller than the points. α represents the spectral index. The peak of the early-time flare occurred at Epoch 4.

The expected geometrical thickness of the shell of hot gas can be approximated as the cooling length ($L_{\rm cool}$; Steinberg & Metzger 2018) where $v_{\rm shock}$ is the shock velocity and $t_{\rm cool}$, for strong shocks, is the time-scale over which compressed gas behind the shock cools radiatively.

$$L_{\rm cool} = v_{\rm shock} t_{\rm cool}/4. \quad (2)$$

Because it is not clear whether the early-time radio flare was the result of the forward or reverse shock, we take $v_{\rm shock}$ to be the velocity of the forward shock. The reverse shock was directed into the fast moving, low-density ejecta and thus had a higher velocity than the forward shock which was directed into higher density ejecta. This lower forward-shock velocity ends up being a more conservative estimate for $v_{\rm shock}$ (see Fig. 4 for a comparison between $M_{\rm hot,needed}$

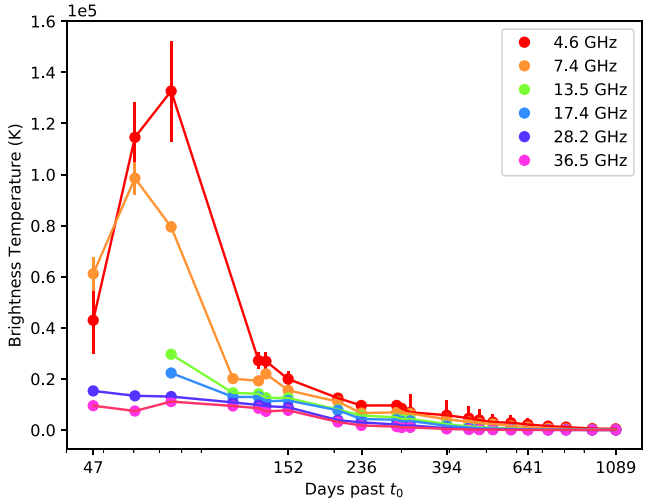

Figure 3. Brightness temperature as a function of time for each of the frequencies at which VLA observed V809 Cep using $D = 6.5$ kpc and source size described in text. The high brightness temperature in the first 3 months after eruption constitutes possible evidence for non-thermal emission and shocks.

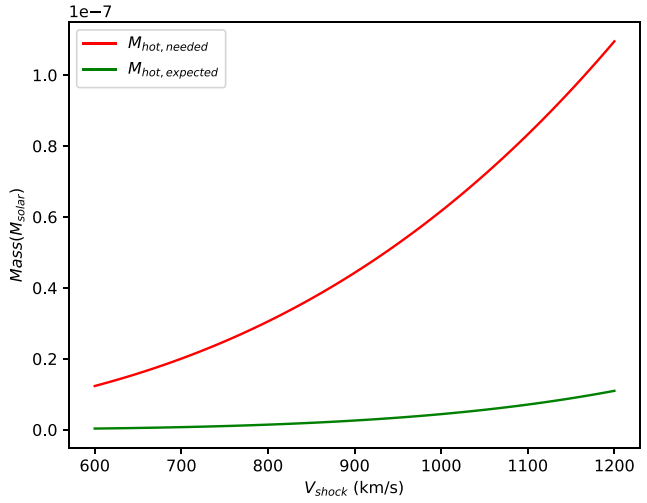

Figure 4. The mass expected in the 10^5 K hot shell between the shocks ($M_{\rm hot,expected}$) and the hot-shell mass needed to explain the early-time flare with just thermal emission ($M_{\rm hot,needed}$) for a range of shock velocities from 600 to 1200 km s^{-1}.

and $M_{\rm hot,expected}$ as a function of $v_{\rm shock}$). The maximum velocity of the principal absorption system seen in optical spectroscopy was 1200 km s^{-1}, and the lowest expansion velocity observed was 600 km s^{-1} (Munari et al. 2014); therefore, we assume a shock velocity between 600 and 1200 km s^{-1}. As gas behind the shock cools radiatively, $t_{\rm cool}$ is given by (Steinberg & Metzger 2018)

$$t_{\rm cool} = \frac{(3/2)\bar{\mu}k_{\rm b}T_{\rm shock}}{\mu_{\rm p}\mu_{\rm e}n_{\rm shock}\Lambda}, \quad (3)$$

where $n_{\rm shock}$ is the number density of the shock compressed gas and the mean molecular weight is $\bar{\mu} = 0.74$ for a typical composition of a fully ionized classical nova ejecta (Vlasov et al. 2016; Sokolovsky et al. 2020; $\mu_{\rm p} = 1.39$ and $\mu_{\rm e} = 1.16$). From Steinberg & Metzger (2018), we estimate the value of the cooling function (Λ) for 10^5 K gas to be 10^{-20} erg cm^3 s^{-1}. Assuming $\bar{\mu} = 0.74$, the temperature of the shock, $T_{\rm shock}$, is related to the shock velocity as (Steinberg & Metzger 2018)

$$T_{\rm shock} \approx 1.7 \times 10^7\ {\rm K} \left(\frac{v_{\rm shock}}{10^3\ {\rm km\ s^{-1}}}\right)^2. \quad (4)$$

We determine $n_{\rm shock} = 4n$ (from the standard shock jump conditions; Steinberg & Metzger 2018) using the total ejecta mass determined from the late-time radio evolution (Section 4.4) and a $1/r^2$ density profile (where r is the distance from the white dwarf) (Weston et al. 2016a). Using $R_{\rm shock} = v_{\rm shock}t$, we find the number density at the location of the shell on day 76. Fig. 4 displays $M_{\rm hot,expected}$ for an appropriate range of shock velocities where $M_{\rm hot,expected}$ was determined by multiplying the mean molecular weight by the expected shell thickness ($L_{\rm cool}$) and number density at the location of the shell. We find that $M_{\rm hot,expected}$ likely fell between 10^{-10} and 10^{-8} M$_\odot$.

For the early-time flare to have been due to thermal emission from gas enclosed within $L_{\rm cool}$, that gas must either have been optically thick with a temperature in excess of $T_{\rm b} = 1.3 \times 10^5$ K or had an even higher temperature. To estimate $M_{\rm hot,needed}$, we assume the hot shell expanded with velocity $v_{\rm shock}$ and is optically thick. The emission measure is EM $= \int_{r_{\rm o}}^{r_{\rm i}} n_{\rm e}^2\, {\rm d}l$, where $n_{\rm e}$ is the electron density, and $r_{\rm o}$ and $r_{\rm i}$ are the outer and inner radii, respectively. We set $r_{\rm o} - r_{\rm i} = L_{\rm cool}$ and $r_{\rm o} = v_{\rm shock}t$. Following Bode & Evans (2008), we calculate the emission measure needed to make the hot shell optically thick ($\tau_\nu = 1$) from

$$\tau_\nu = 1 = 8.235 \times 10^{-2} \left(\frac{T_{\rm e}}{K}\right)^{-1.35} \left(\frac{\nu}{\rm GHz}\right)^{-2.1} \frac{{\rm EM}(\tau_\nu)}{\rm cm^{-6}\ pc}. \quad (5)$$

By setting $\tau_\nu = 1$ in the expression for the emission measure and taking a constant density profile within the hot shell, we derive the number density of electrons needed to make a $T_{\rm e} \sim 10^5$ K shell optically thick at 4.55 GHz. As with $M_{\rm hot,expected}$, we multiply the number density by the mean molecular weight by the expected shell thickness ($L_{\rm cool}$) to obtain $M_{\rm hot,needed}$. Fig. 4 shows both $M_{\rm hot,expected}$ and $M_{\rm hot,needed}$ enclosed in a shell of thickness $L_{\rm cool}$ as a function of shock velocity.

For $v_{\rm shock}$ between 600 and 1200 km s^{-1}, $M_{\rm hot,needed}$ exceeded $M_{\rm hot,expected}$ by at least an order of magnitude. For $v_{\rm shock}$ of 900 km s^{-1}, $M_{\rm hot,needed} = 1.5 \times 10^{-8}$ M$_\odot$ and $M_{\rm hot,expected} = 8.5 \times 10^{-10}$ M$_\odot$. It is thus implausible for the high brightness temperature to have been the result of thermal emission from a shock-heated shell. This finding further supports our assertion that the high brightness temperature is most likely the result of non-thermal emission produced in a shock.

Non-thermal emission from classical novae is widely accepted to be the result of internal shocks in the ejecta (O'Brien & Lloyd 1994; Vlasov et al. 2016; Weston et al. 2016a; Finzell et al. 2018; Franckowiak et al. 2018; Chomiuk et al. 2021). The collision of the fast and slow flows results in shocks that are responsible for accelerating particles to relativistic speeds. Novae V1723 Aql (Weston et al. 2016a), V5589 Sgr (Weston et al. 2016b), and nova 1324 Sco (Finzell et al. 2018) had brightness temperatures of greater than 10^5 K, interpreted as evidence for radio synchrotron emission from shocks. We similarly propose that the bright radio emission that the VLA detected on 2013 April 19 (Epoch 4) was the result of shocks in ejecta from V809 Cep. V809 Cep thus joins six other classical novae with radio evidence for shocks: V906 Car (Aydi et al. 2020b), V1324 Sco (Finzell et al. 2018), V1723 Aql (Weston et al. 2016a), V5589 Sgr (Weston et al. 2016b), V959 Mon (Chomiuk et al. 2014a), and QU Vul (Taylor et al. 1987). Non-thermal radio emission has also been found in the eruptions of closely related objects including the helium nova V445 Pup (Nyamai et al. 2021) and the symbiotic system V407 Cyg (Giroletti et al. 2020).

4.2 Spectral evolution

The radio spectral evolution during the rise to maximum of the early-time flare in V809 Cep had some resemblance to theoretical predictions for synchrotron from internal shocks in novae by Vlasov et al. (2016). Those authors suggested that photoionized gas ahead of the shock initially absorbs radio synchrotron emission, causing the spectral index (α) to evolve from approximately 2.0, as expected for optically thick thermal emission, to 2.5 when the photoionized gas ahead of the shock becomes transparent and optically thick synchrotron emission begins to dominate the spectrum. Vlasov et al. (2016) predicted that the spectral index then gradually decreases toward the $\alpha = -0.7$ expected for optically thin synchrotron (the exact value depends on the energy spectrum of the emitting particles, e.g. Pacholczyk 1970). Later, the spectral index is expected to once again rise as the radio emission becomes dominated by optically thick thermal emission from the bulk of the expanding, photoionized ejecta. The peak of the early-time flare occurs as the synchrotron transitions from optically thick to optically thin (Vlasov et al. 2016).

At low frequencies (below 7.4 GHz), the radio emission during the early-time flare in V809 Cep was consistent with theoretical expectations – if the VLA began detecting the flare when photoionized gas ahead of the shock had already become partially transparent. During the flare, the low-frequency spectral index transitioned from a high value suggestive of optically thick synchrotron emission (2.8 ± 0.7 in Epoch 2) to the more modest value of 0.5 ± 0.1 at the peak of the flare (during Epoch 4). Though the error bars on the low-frequency spectral index at Epoch 2 are large, in combination with the high brightness temperature, the high spectral index implies optically thick synchrotron emission.

The flattening of the low-frequency spectral index at Epoch 4 suggests that the spectrum was indeed transitioning from one indicative of optically thick to optically thin synchrotron emission at that time, as predicted by Vlasov et al. (2016). At Epoch 5, the low-frequency spectral index increased again, to 1.58 ± 0.05, as expected for optically thick thermal emission from the main, expanding ejecta beginning to dominate over the early-time synchrotron emission.

At high frequencies, the radio emission during the early-time flare can also be understood within the framework of Vlasov et al. (2016). Synchrotron emission from an expanding medium is expected to become optically thin, and the spectral index to decrease, at the highest frequencies first (29 GHz and above, in our case). The high-frequency spectral indices at Epochs 2 and 3 of 0.1 ± 0.4 and -0.3 ± 0.2, respectively, thus follow the spectral evolution modelled in Vlasov et al. (2016) if the synchrotron emission had already become fairly optically thin at those frequencies by Epochs 2 and 3. Moreover, because the high-frequency radio spectrum was already quite flat when the VLA first detected the source in Epoch 2, with the high-frequency flux densities well below an extrapolation of the low-frequency spectrum at that time, synchrotron emission at frequencies higher than 7.4 GHz likely peaked before it peaked at low frequencies, and even prior to the first radio detection. Further supporting the possibility that any synchrotron peaked at high frequencies before low frequencies, at 7.4 GHz, the brightness temperature peaked during Epoch 3, an epoch before the peak at 4.6 GHz. Brightness temperature represents a lower limit on the physical temperature of an optically thin gas; therefore, we expect the brightness temperature to peak at high frequencies prior to peaking at low frequencies as the high frequencies become optically thin first. Fig. 3 displays a peak first at Epoch 3 (day 61) at 7.4 GHz and later at Epoch 4 (day 76) at 4.6 GHz. We thus posit that the early-time flare peaked at high frequencies prior to the first radio detection.

Absorption by photoionized gas ahead of the shock would initially obscure the non-thermal emission and produce a delay between the early-time radio maxima at progressively lower frequencies (Vlasov et al. 2016). As the photoionized gas ahead of the shock begins to diffuse and become optically thin at lower frequencies, the non-thermal emission from the shock becomes increasingly dominant first at higher frequencies and finally at lower frequencies. So, hints that the synchrotron flare peaked at higher frequencies first (rather than at all frequencies simultaneously) suggest that non-thermal emission from internal shocks in the V809 Cep ejecta was initially absorbed by photoionized gas ahead of the shock. However, even if any synchrotron emission was initially somewhat absorbed by photoionized gas, the high spectral index of 2.8 ± 0.7 during Epoch 2 (day 48) would indicate that we caught the flare when the putative synchrotron emission was already peeking through at low frequencies.

The radio spectral evolution during Stage 2 (Epochs 5–9 – see Section 3 for stages) further supports our assertion that the spectrum during stage 1 was attributable to an emission component that was physically distinct from the main photoionized ejecta. As the early emission component thinned, the radio spectrum became increasingly dominated by optically thick thermal emission. Indeed, during Epochs 4 (day 76), the spectral index at high frequencies rose to 1.5 ± 0.1, indicative of optically thick thermal emission. During Epoch 5 through 9 (days 110–206), the spectral index for all frequencies increased to 1.58 ± 0.05 and remained around 1.5 as the ejecta expanded and the radio emission brightened for the remainder of stage 2. Although the stage 2 spectral indices were lower than the expected 2.0 for optically thick thermal emission from a medium with an infinitely sharp outer edge, values of 1.5 are typical for actual nova remnants. Therefore, the radio spectral evolution was consistent with emission from an increasingly optically thin synchrotron source and a gradually brightening optically thick thermal component. During stages 3 and 4, the radio spectrum was typical of a thermal source becoming increasingly optically thin, with the spectrum flattening at progressively lower frequencies as gas began to become optically thin first at high frequencies (>29 GHz) and by Epoch 20 (day 726) at all frequencies.

4.3 Quasi-simultaneity of synchrotron flare and dust formation

Around the start of the early-time flare, dust production also commenced, providing evidence for a connection between shocks and dust formation. In the shock–dust model (Derdzinski et al. 2017), internal shocks in the ejecta lead to dust condensation. We would naively expect, therefore, to see evidence for the shocks *prior* to the onset of dust formation, which began around 2013 March 11 (day 37; Munari et al. 2014). The VLA did not observe V809 Cep between day 12 (Epoch 1) and day 48 (Epoch 2) of the eruption, so we cannot pinpoint the exact time at which synchrotron emission appeared (or peaked at high frequencies). But on day 48 (Epoch 2), 11 d past the onset of dust formation, we detected radio emission almost certainly associated with shocks within the ejecta. Therefore, both signatures of shocks and dust appeared during the 1 month gap between Epoch 1 (day 12) and Epoch 2 (day 48) (Table 3). Given the evidence that the early-time flare did not peak at the same time at all frequencies and therefore that any synchrotron was initially obscured, the radio observations are consistent with the shocks arising either slightly before or around the same time as the onset of dust production.

Table 3. V809 Cep timeline.

Event	Date	$t - t_0$[a]
Optical detection[a]	2013 February 2	0
Optical peak	2013 February 3	1
Onset of dust production	2013 March 11	37
Synchrotron detected	2013 March 22	48
Peak of low-frequency synchrotron	2013 April 19	76

[a]Days past t_0 of the eruption on 2013 February 2.

4.4 Properties of the thermal ejecta

Starting about 9 months into the eruption, the radio emission was reasonably consistent with bremsstrahlung (free–free emission) from freely expanding, photoionized ejecta. We modelled the main ejecta as a Hubble flow (Seaquist & Palimaka 1977; Hjellming et al. 1979; Gehrz 2008; Weston et al. 2016a; Finzell et al. 2018), in which the ejecta consists of a homologously expanding isothermal spherical shell of gas bound between inner and outer radii $r_{\rm inner}$ and $r_{\rm outer}$, with a r^{-2} density profile (where r is the distance from the white dwarf), and a volume filling factor, f. The filling factor is a measure of inhomogeneities in the ejecta, such as clumps (e.g. Hjellming 1996; Weston et al. 2016a). We assume no inhomogeneities ($f = 1$). If the ejecta were actually clumpy, that would reduce the ejecta mass needed to generate the observed radio emission (Abbott, Bieging & Churchwell 1981; Leitherer & Robert 1991; Hjellming 1996; Chomiuk et al. 2014b; Weston et al. 2016a).

At low frequencies (<7.4 GHz) during the first 6 months or so of the outburst, the model fits the observed flux densities poorly and, as expected, was unable to account for the early-time flare. At 13.5 and 17.0 GHz, the discrepancy between the model and the observed flux densities during the first few months of the eruption supports our contention (in Section 4.2) that the flare at these frequencies could have peaked before Epoch 4 (day 76). At these frequencies, the Hubble flow model matched the observed flux densities well after Epoch 4 (day 76). At Epoch 4 (day 76), however, the observed flux density at 17.4 GHz was 0.94 ± 0.02 mJy, 0.61 mJy in excess of the model flux density of 0.33 mJy. At 13.5 GHz, the observed flux density was 0.789 ± 0.002, 0.58 mJy in excess of the model flux density. The observed flux densities of 13.5 and 17.4 GHz were far in excess of the model during Epoch 4 (day 76) indicates that any synchrotron emission was still dominant at those frequencies at that time and could therefore have peaked even earlier [the VLA did not collect data at these frequencies during Epochs 2 and 3 (days 48 and 61)].

At 28.8 and 36.5 GHz, and after approximately days 200–300 (>Epoch 10) at all frequencies, however, the model reproduces the observed flux densities moderately well. Using $D = 6.5$ kpc, $v_{\rm ej} = 1200$ km s^{-1}, and $v_{\rm min} = 600$ km s^{-1}, we determined the best-fiting ejecta mass and temperature by employing the Markov chain Monte Carlo program PYMC. We found $M_{\rm ejected} = (1.1 \pm 0.1) \times 10^{-4}$ M$_\odot$ and $T = (0.8 \pm 0.2) \times 10^4$ K when the Hubble flow model was fit to the flux densities starting from Epoch 2 (day 48) (first detection). As the Hubble flow model is unable to account for the early-time flare, we also fit the model excluding the early-time flare (Epochs 2–4) at 4.6 and 7.4 GHz; however, we found similar values for $M_{\rm ejected}$ and T. Fig. 5 displays the observed flux densities as well as the modelled free–free emission for $D = 6.5$ kpc, $M_{\rm ejected} = (1.1 \pm 0.1) \times 10^{-4}$ M$_\odot$, and $T = (0.8 \pm 0.2) \times 10^4$ K.

Fig. 5 displays a deviation between the Hubble flow model and the flux densities between Epochs 9 and 11 (days 206–293) at 36.5, 28.2, and 17.4 GHz. This additional structure in the radio light curve could be evidence for multiple thermal outflows, hints of which are seen in optical spectra of novae (Aydi et al. 2020a). Further discussion is beyond the scope of this paper.

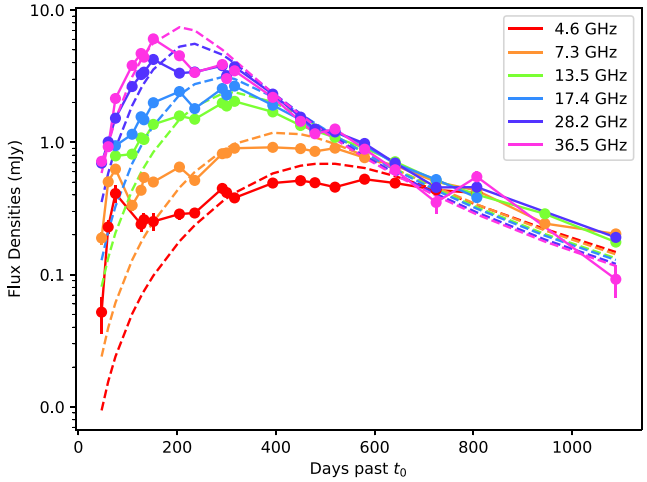

Figure 5. Hubble flow model compared with observed flux densities. The dashed lines show the model flux densities, and the solid points denote the observed flux densities. The model fluxes are calculated using $M_{\rm ejected} = 1.1 \times 10^{-4}$ M$_\odot$, $T = 0.8 \times 10^4$ K, $v_{\rm ej} = 1200$ km s^{-1}, $v_{\rm min} = 600$ km s^{-1}, and $D = 6.5$ kpc.

5 CONCLUSIONS

(i) The radio light curves at 4.6 and 7.4 GHz display an early-time flare that peaks at Epoch 4 (day 76). At 4.6 GHz, the brightness temperature at that time was at least 1.5×10^5 K.

(ii) At low frequencies (<7.4 GHz), the rise of the early-time flare began at Epoch 2 (day 48, 2013 March 22). The spectral index at low frequencies at Epoch 2 (day 48) was 2.82 ± 0.71.

(iii) The high brightness temperature at the peak of the early-time flare at Epoch 4 (day 76) combined with the high spectral index at Epoch 2 (day 48) suggests the presence of non-thermal emission due to internal shocks in the nova ejecta. This is the first report showing evidence for shocks in V809 Cep.

(iv) The discovery of non-thermal radio emission early in the evolution of the eruption puts V809 Cep in the same category as six other novae known to show radio evidence for shocks: V906 Car (Aydi et al. 2020b), V1324 Sco (Finzell et al. 2018), V1723 Aql (Weston et al. 2016a), V5589 Sgr (Weston et al. 2016b), V959 Mon (Chomiuk et al. 2014a), and QU Vul (Taylor et al. 1987).

(v) At late times [after Epoch 4 (day 76)], the radio emission was consistent with thermal emission from freely expanding ejecta with a maximum ejecta speed of 1200 km s^{-1}, $v_{\rm min} = 600$ km s^{-1}, $D = 6.5$ kpc, $T = 0.8 \times 10^4$ K, and $M_{\rm ejected} = 1.1 \times 10^{-4}$ M$_\odot$.

(vi) Our finding that a radio synchrotron flare associated with internal shocks in the ejecta began during a roughly month-long period of time during which dust formation also commenced supports the idea that shocks could form ideal environments for dust formation around novae.

(vii) If shocks in the nova ejecta lead to dust formation, the 11-d delay between the onset of dust and the rise of the early-time flare suggests that the radio emission was absorbed by photoionized gas ahead of the shock.

ACKNOWLEDGEMENTS

The National Radio Astronomy Observatory is a facility of the National Science Foundation operated under cooperative agreement by Associated Universities, Inc. AB and JLS acknowledge support from US National Scence Foundation (NSF) grant AST-1816100 and Heising-Simons Foundation grant 2017-246, as well as US National Radio Astronomy Observatory Student Observing Support Award 362918. LC, AMK, EA, and KVS were supported by NSF grant AST-1751874 and a Cottrell fellowship of the Research Corporation.

DATA AVAILABILITY

The data underlying this article will be shared on reasonable request to the corresponding author. The uncalibrated radio observations are publicly available from the NRAO Data Archive (archive.nrao.edu or data.nrao.edu).

REFERENCES

Abbott D. C., Bieging J. H., Churchwell E., 1981, ApJ, 250, 645
Ackermann M. et al., 2014, Science, 345, 554
Atwood W. B. et al., 2009, ApJ, 697, 1071
Aydi E. et al., 2020a, ApJ, 905, 62
Aydi E. et al., 2020b, Nat. Astron., 4, 776
Blandford R. D., 1994, ApJS, 90, 515
Bode M. F., Evans A., 2008, Classical Novae. Cambridge Univ. Press, Cambridge
Brand J., Blitz L., 1993, A&A, 275, 67
Buson S., Jean P., Cheung C. C., 2019, Astron. Telegram, 13114, 1
Chomiuk L. et al., 2014a, Nature, 514, 339
Chomiuk L. et al., 2014b, ApJ, 788, 130
Chomiuk L., Metzger B. D., Shen K. J., 2021, ARA&A, 59, 391
Cunningham T., Wolf W. M., Bildsten L., 2015, ApJ, 803, 76
Della Valle M., Izzo L., 2020, A&AR, 28, 3
Derdzinski A. M., Metzger B. D., Lazzati D., 2017, MNRAS, 469, 1314
Downes R. A., Duerbeck H. W., 2000, AJ, 120, 2007
Evans A., 2001, Ap&SS, 275, 131
Finzell T. et al., 2018, ApJ, 852, 108
Franckowiak A., Jean P., Wood M., Cheung C. C., Buson S., 2018, A&A, 609, A120
Gallagher J. S., 1977, AJ, 82, 209
Gehrz R. D., 2008, Infrared Studies of Classical Novae, 2 edn. Cambridge Univ. Press, Cambridge, p. 167
Giroletti M. et al., 2020, A&A, 638, A130
Greisen E. W., 2003, Information Handling in Astronomy. Kluwer Academic Pbl., Dordrecht, p. 109
Hjellming R. M., 1996, in Taylor A. R., Paredes J. M., eds, ASP Conf. Ser. Vol. 93, Radio Emission from the Stars and the Sun. Astron. Soc. Pac., San Francisco, p. 174
Hjellming R. M., Wade C. M., Vandenberg N. R., Newell R. T., 1979, AJ, 84, 1619
Leitherer C., Robert C., 1991, ApJ, 377, 629
Li K.-L. et al., 2017, Nat. Astron., 1, 697
Martin P., Dubus G., Jean P., Tatischeff V., Dosne C., 2018, A&A, 612, A38
McMullin J. P., Waters B., Schiebel D., Young W., Golap K., 2007, in Shaw R. A., Hill F., Bell D. J., eds, ASP Conf. Ser. Vol. 376, Astronomical Data Analysis Software and Systems XVI. Astron. Soc. Pac., San Francisco, p. 127
Metzger B. D., Finzell T., Vurm I., Hascoët R., Beloborodov A. M., Chomiuk L., 2015, MNRAS, 450, 2739
Metzger B. D., Caprioli D., Vurm I., Beloborodov A. M., Bartos I., Vlasov A., 2016, MNRAS, 457, 1786
Munari U. et al., 2014, MNRAS, 440, 3402
Nyamai M. M., Chomiuk L., Ribeiro V. A. R. M., Woudt P. A., Strader J., Sokolovsky K. V., 2021, MNRAS, 501, 1394
O'Brien T. J., Lloyd H. M., 1994, Ap&SS, 216, 167
Pacholczyk A. G., 1970, Radio Astrophysics. Nonthermal Processes in Galactic and Extragalactic Sources. Freeman, San Francisco
Seaquist E. R., Palimaka J., 1977, ApJ, 217, 781
Shore S. N., Kuin N. P., Mason E., De Gennaro Aquino I., 2018, A&A, 619, A104
Sokolovsky K. V. et al., 2020, MNRAS, 497, 2569
Starrfield S., Iliadis C., Hix W. R., 2016, PASP, 128, 051001
Steinberg E., Metzger B. D., 2018, MNRAS, 479, 687
Strope R. J., Schaefer B. E., Henden A. A., 2010, AJ, 140, 34
Taylor A. R., Seaquist E. R., Hollis J. M., Pottasch S. R., 1987, A&A, 183, 38
Vlasov A., Vurm I., Metzger B. D., 2016, MNRAS, 463, 394
Weston J. H. S. et al., 2016a, MNRAS, 457, 887
Weston J. H. S. et al., 2016b, MNRAS, 460, 2687

This paper has been typeset from a TEX/LATEX file prepared by the author.